The Role of Longwave Radiation and Boundary Layer Thermodynamics in Forcing Tropical Surface Winds*

XIOUHUA FU AND BIN WANG

Department of Meteorology, School of Ocean and Earth Science and Technology, University of Hawaii at Manoa, Honolulu, Hawaii

ABSTRACT

This paper reveals major deficiencies of the existing intermediate climate models for tropical surface winds and elaborates the important roles of cloud-longwave radiational forcing and boundary layer thermodynamics in driving the tropical surface winds.

The heat sink associated with the cloud-longwave radiation is demonstrated as an important driving force for boreal summer northeast trades and Indian Ocean southwest monsoons. Over the western North Pacific and Atlantic Oceans, low cloudiness and high sea surface temperature enhance longwave radiation cooling, strengthening subtropical high and associated trades. On the other hand, in the regions of heavy rainfall over South Asia, reduced cloud-longwave radiation cooling enhances monsoon trough and associated southwest monsoons. The boundary layer thermodynamic processes, primarily both the surface heat fluxes and the vertical temperature advection, are shown to be critical for a realistic simulation of the intertropical convergence zone, the equatorial surface winds, and associated divergence field.

To successfully simulate the tropical surface winds, it is essential for intermediate models to adequately describe the feedback of the boundary layer frictional convergence to convective heat source, cloud-longwave radiation forcing, boundary layer temperature gradient forcing, and their interactions. The capability and limitations of the intermediate tropical climate model in reproducing both climatology and interannual variations are discussed.

1. Introduction

The work of Gill (1980) demonstrated the capability of a single–baroclinic-mode model in simulation of elementary features of tropical circulations in response to a specified heat source. The success of the Gill model leads to its popular applications in simple and intermediate climate models for simulation of atmospheric anomalous response to underlying SST anomalies (SSTA). In anomaly models, diabatic heating was simply related to SSTA by considering anomalous surface latent heat flux and low-level moisture convergence (e.g., Zebiak 1982, 1986), and/or Newtonian cooling (e.g., Davey and Gill 1987). Seager (1991) extends this type of anomaly model to simulate the tropical total surface wind field. The diabatic heating in his model was determined by a simple convective scheme in the spirit of Betts and Miller (1986). The resultant heating

was essentially controlled by low-level moisture convergence, which is a feature similar to that of a simplified Kuo's (1974) scheme. The simulated large-scale surface winds compare, in many aspects, favorably to the observations. The trade winds, however, are much too zonal with a severe shrinkage in the area of the northeast trades over the North Pacific and Atlantic Oceans in boreal summer; the convergence is considerably weaker in the intertropical convergence zones (ITCZs).

In contrast to Gill (1980) model dynamics, Lindzen and Nigam (1987, LN hereafter) emphasized the role of SST gradients in driving low-level flows: The SST gradients induce pressure gradient force via vertical turbulent mixing and hydrostatic balance in the planetary boundary layer (PBL). The LN model was able to produce a reasonable low-level flow field without explicitly considering convective heating. But the convergent air mass in the boundary layer has to be assumed being vented out of PBL by cumulus on a very short timescale (about 30 min) and the boundary layer depth has to be assumed 3 km deep in order to obtain a reasonable strength (Wang and Li 1993). The simulated spatial pattern of sea level pressure (SLP) follows SST distribution much too closely, resulting in an SLP field that is considerably different from the observed counterpart in the eastern Pacific and Atlantic Oceans. Although the dy-

Corresponding author address: Dr. Bin Wang, Department of Meteorology, University of Hawaii at Manoa, 2525 Correa Road, Honolulu, HI 96822.
E-mail: bwang@loihi.soest.hawaii.edu

namics in the LN model differ fundamentally from those in Gill-type model, their formulations are mathematically equivalent (Neelin 1989). Deficiencies of the two types of models are essentially the same.

In view of the importance of the boundary layer flow in supplying moist static energy to convective heating and interacting with ocean, Wang and Li (1993, WL93 hereafter) developed a two–vertical-mode model that describes the lowest baroclinic mode of the free troposphere and the barotropic boundary layer mode. The model integrates the physics of Gill and LN models and emphasizes the roles of the interaction between heating-forced free tropospheric motion and SST gradient-forced PBL flows in driving the tropical surface winds. The model can reproduce both the shallow ITCZ and the deep South Pacific convergence zone (SPCZ). The simulation of ITCZ and trades is more realistic, but the surface wind divergence in the equatorial eastern Pacific is excessively strong and the summer trades remain significantly weak.

Simulation of oceanic monsoon flows is a challenging task faced by the intermediate tropical climate models. Using a six-level primitive equation model with Betts–Miller (1993) convective adjustment scheme and Deardorff's (1972) boundary layer parameterization, Seager and Zebiak (1995) obtain improved simulation of tropical circulations. Nevertheless, the simulated Indian monsoon and the cross-equatorial winds over the eastern Atlantic and Pacific Oceans remain unsatisfactory.

An optimal intermediate tropical climate model should describe only the essential physical processes that govern tropical circulations, with most suitable formulations under the constraints of limited degree of freedom. Any improvement should preserve the virtues of intermediate models: the intelligibility for understanding essential physics, the efficiency in conducting numerical experiments, and the comparability of the results with observations. For the above reasons, our thinking is to first identify the processes that are critical to simulation of tropical surface winds but are inadequately represented in the existing intermediate models, then correct or implement the intermediate model physics.

In the next section, we diagnose the deficiencies of the WL93 model and identify two major processes that are responsible for the deficiencies: the misrepresentation of cloud-longwave radiation forcing and the PBL SST gradient forcing. We then improve the model based on physical principles while conforming with the constraint of the model's degree of freedom (sections 3 and 4). Results of sensitivity experiments indicate that the heat sink associated with longwave radiation cooling plays an important role in driving tropical circulations (especially causing the westward phase shift of subtropical highs relative to cold SST tongues). The improvement of longwave radiation results in a much better simulation of trade winds and monsoons in boreal summer. In addition, PBL adiabatic warming associated

with vertical motion is shown to be important for the reasonable simulation of the equatorial wind divergence fields. The performance and potential of the improved WL model in simulations of tropical climatological annual cycle and interannual variability are critically examined in section 5. The last section summarizes the major results.

2. Deficiencies of the existing intermediate tropical climate models

To diagnose the problems of the existing intermediate models, we select WL93 model for the following two reasons. First, it contains the essential dynamics of the Gill and LN models and has the capability of simulation of both the climatology and interannual variations. Second, the deficiencies of the model, as discussed in detail shortly, are shared by other intermediate models.

a. The intermediate tropical climate model

The WL93 model is a two and one half layer primitive equation model on the equatorial beta plane. It was aimed at simulating monthly mean tropical surface winds, SLP, and rainfall for specified lower boundary conditions. A detailed description of model physics and formulations is given by Wang and Li (1993). The convective latent heating in the WL93 model is not only controlled by large-scale circulations but also the convective instability associated with SST. Therefore, the latent heating is determined by the precipitational rate P_r, which is parameterized as a fraction, b, of the total column moisture convergence following Kuo (1974), and is regulated by the in situ convective instability. The convective instability parameter δ is a function of SST (or land surface air temperature, T_s) based on the observation of Waliser et al. (1993):

$$\delta = \begin{cases} 1, & \text{if } T_s \geq 27°C \quad \text{and} \quad P_r > 0, \\ (T_s - 25)/2, & \text{if } 25°C < T_s < 27°C \quad \text{and} \quad P_r > 0, \\ 0, & \text{otherwise.} \end{cases}$$

$$(2.1)$$

The original model, which was confined to the tropical Pacific Ocean, is extended to the global Tropics between 30°S and 30°N. The surface temperature used is the observed SST (Reynolds 1988) over the ocean and the 1000-mb air temperature [European Centre for Medium-Range Weather Forecasts (ECMWF) analysis] over the land. In coastal regions the Shuman-smoothing scheme (Shuman 1957) is used to provide continuity. The resultant observed July mean surface temperature is presented in Fig. 1a. The surface specific humidity q_0 and evaporation rate E_v are empirically parameterized as

$$q_0 = m_a 10^{-3}(0.972T_s - 8.92), \quad (2.2)$$
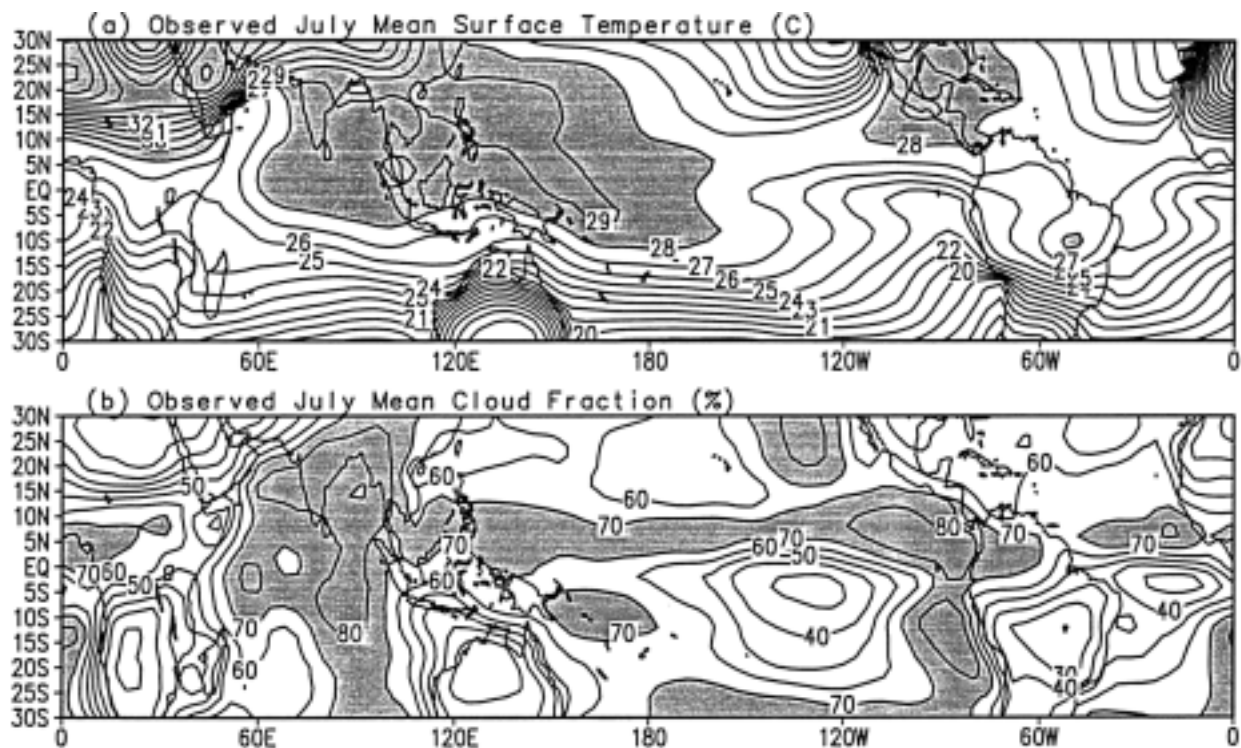
$$E_v = m_a \rho C_E V_s(q_s - q_0), \quad (2.3)$$

FIG. 1. (a) Observed July mean surface temperature (°C) and (b) cloud fractions (%). The sea surface temperature is from Reynolds (1988), while the land surface temperature is the 1000-mb air temperature from ECMWF analysis. The cloud fraction is derived from ISCCP.

where T_s is the surface temperature; ρ and C_E are surface air density and coefficient of vertical turbulent moisture flux, respectively; q_s is the saturation specific humidity at the surface temperature T_s; V_s is the surface wind speed (a minimum wind speed is set as 4 m s^{-1}). Over ocean surfaces, moisture availability m_a is equal to one, thus Eqs. (2.2) and (2.3) recover the empirical formula used for the Pacific regional model (WL93) that were derived from the regression analysis of Comprehensive Ocean–Atmosphere Data Set (COADS) monthly mean SST and surface specific humidity (Wang 1988; Li and Wang 1994). Over land surfaces, m_a is parameterized as a function of surface coverage classified by Matthews (1983). The global tropical surface is divided into eight categories, whose corresponding moisture availability used in the present model is given in Table 1. These values are based on various observational analyses (e.g., Benjamin and Carlson 1986).

The standard horizontal grid is 2° lat × 4° long. In order to keep computational stability, a simulated backward scheme (Matsuno 1966) is used with a time increment of 30 min. Radiational boundary conditions (Miller and Thorpe 1981) are used at the north and south boundaries to eliminate shortwave reflection. The major parameter values used in this model are listed in Table 2.

b. Major deficiencies

To reveal the deficiencies, we focus on a July simulation because nearly all intermediate models produce poorer simulation in boreal summer than in other sea-

TABLE 1. Surface moisture availability as a function of surface coverage.

Surface coverage	Moisture availability
Water	1.0
Rain forest	0.9
Forest	0.85
Woodland	0.8
Shrub land	0.75
Grass	0.7
Agriculture	0.6
Desert	0.02

TABLE 2. The major parameter values used in the model.

|		
b	Precipitation efficiency coefficient	0.8
ε	Rayleigh friction coefficient in free troposphere	5×10^{-6} s^{-1}
β	Meridional gradient of the Coriolis parameter at the equator	2.28×10^{-11} s^{-1} m^{-1}
ρ	Surface air density	1.2 kg m^{-3}
g	Gravity	9.8 m s^{-2}
R	Gas constant of air	287 J kg^{-1} C^{-1}
C_p	Specific heat at constant pressure	1004 J kg^{-1} C^{-1}
S_o	Static stability parameter at the surface	0.75×10^{-6} m^2 s^{-2} Pa^{-2}
C_E	Coefficient of vertical turbulent moisture flux	1.3×10^{-3}
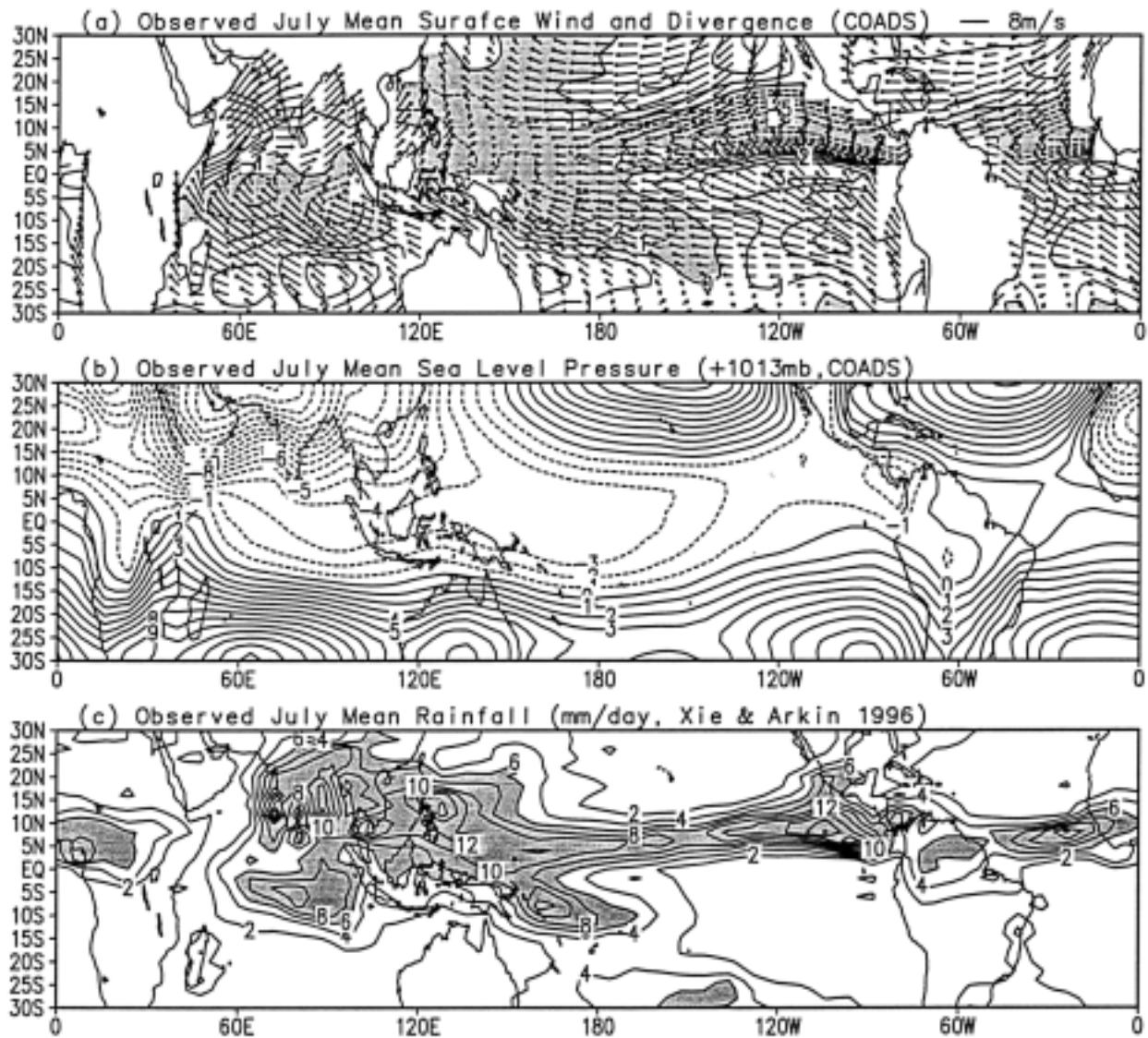
FIG. 2. (a) Observed July mean surface winds and divergence, (b) sea level pressure (SLP), and (c) precipitation. The data used in (a) and (b) are derived from Sadler et al. (1987). Those used in (c) are from Xie and Arkin (1996). The contour interval for divergence, SLP, and rainfall are, respectively, 1×10^{-6} s^{-1}, 1 hPa, and 2 mm day^{-1}. The SLP field is the departure from a mean value 1013 hPa.

sons. Surface winds are the primary concern because surface winds play a crucial role in driving the upper ocean and in regulating the ocean mixed layer in a coupled ocean–atmosphere system. The SLP and rainfall directly link to surface winds. We will target these two fields as well. A number of significant discrepancies between the observed (Fig. 2a) and simulated surface winds (Fig. 3a) can be seen from Fig. 3b: 1) the simulated northeast trades are substantially weak and much too confined to the eastern basins (the largest discrepancy is found over the Caribbean); 2) the simulated southwest monsoon flows over the northern Indian Ocean are notably weak; and 3) the simulated cross-equatorial southeast trades are also significantly weak.

In order to understand the causes of the weak north-

east trades, we examine the simulated SLP (Fig. 3c), which is basically negatively correlated with SST (Fig. 1a) over the tropical oceans. As a result, the subtropical highs over the North Pacific and North Atlantic Oceans are tightly confined to the eastern basins (cf. Figs. 2b and 3c). This is a common problem with Gill and LN models because the surface temperature is the only forcing. From the distribution of cloudiness (Fig. 1b), one finds that the cloud fraction over the western North Pacific and Atlantic Oceans are relatively small. The low cloud fractions and high SST in these regions imply strong outgoing longwave radiation. This was noted in the analyses of Trenberth and Soloman (1994), who indicate that large longwave radiation cooling in July occurs over the North Pacific and North Atlantic Oceans.
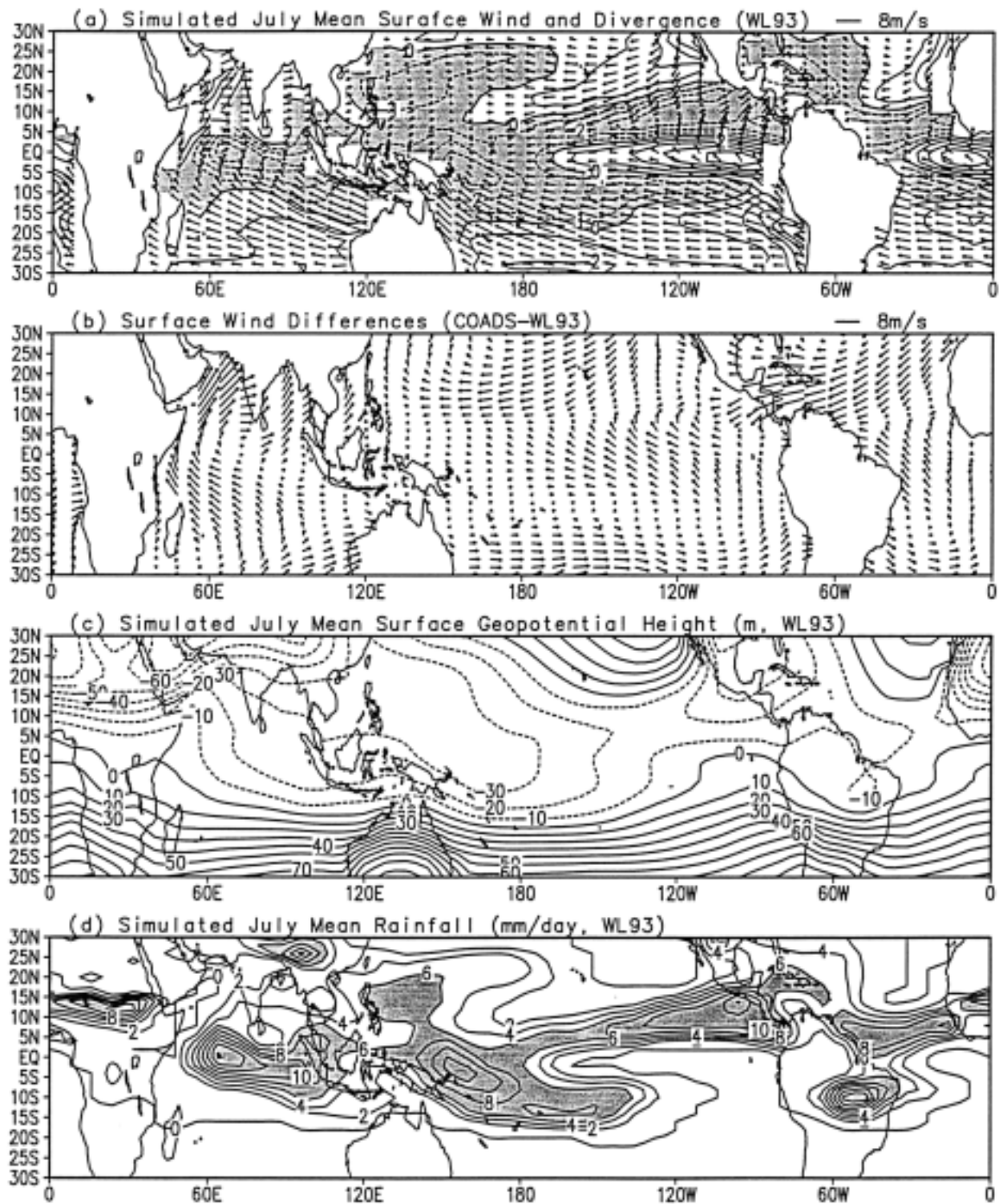
FIG. 3. (a) July mean surface winds and divergence, (b) the differences between the modeled surface winds and observations, (c) the surface geopotential height, and (d) precipitation simulated by original WL93 model.

The model diabatic heating field, however, indicates no diabatic cooling presenting in these regions (figure not shown). Instead, the Newtonian cooling in the WL93 model acts to warm (cool) the atmosphere over high (low) SST regions. Thus, it adds spurious warming to these regions. This directly reduces the strength of the northern subtropical highs in the western North Pacific and Atlantic basins.

Misrepresention of longwave radiational forcing can also be the cause of the underestimated southwest monsoons in the Indian Ocean. This is because, in reality, the precipitating cloud-induced longwave radiation forcing in the rainy regions tends to warm the atmosphere, whereas the Newtonian cooling in the WL93 model and other Gill-type models acts to offset the warming due to latent heat release. As such, the Newtonian cooling would prohibit the decrease of SLP in the precipitating regions (South Asia), resulting in a weaker north–south pressure gradient and southwest monsoon flows.

Why are the cross-equatorial southeast trades in the Pacific and Atlantic Oceans weaker than the observations? Computation of meridional pressure gradients (figure not shown) reveals that the simulated meridional pressure gradient is positive just south of the equator over the eastern Pacific and Atlantic Oceans, which is at odds with the observations. This positive pressure gradient, though very small, resists southeast trades and significantly weakens the cross-equatorial flows. We have further diagnosed the contributions of the free troposphere and PBL forcing to these positive SLP gradients and found that they are primarily attributed to the PBL forcing. The latter are caused by SST gradients associated with the cold SST tongue. Therefore, we speculate that, over the eastern Pacific and Atlantic Oceans, the slab mixing layer assumption might exaggerate the effects of SST gradient forcing on surface flows. As a result, the cross-equatorial southeast trades weaken, which induces a spurious surface convergence zone on the south side of the equator (Fig. 3a). With the SST forcing in the slab PBL model, the cold water off the Somalia coasts (Fig. 1a) produces an overestimated pressure ridge in the western equatorial Indian Ocean (Fig. 3c). A belt of positive meridional pressure gradient exists between 5° and 10°N across the Indian Ocean, which tends to split the summer rainfall region into a northern and an equatorial patch, leaving deficit monsoon rain over the Indian subcontinent and the Bay of Bengal (Fig. 3d). It seems that the slab PBL model exaggerates the effects of SST gradients, which is in turn responsible for the problems in the simulation of the surface wind divergence, the associated rainfall, and Indian monsoon.

The above analysis suggests that the major problems of July simulations with the WL93 model are possibly induced by 1) misrepresentation of the longwave radiation, and 2) oversimplification of the PBL model. In the following two sections, we will improve the WL93 model and test the impacts of the modified longwave radiation forcing and PBL processes on the simulations of the global tropical surface winds.

3. The role of cloud-longwave radiation forcing

a. The new longwave radiation scheme

In the previous intermediate climate models, longwave radiative heating was often simply treated as a Newtonian cooling, relaxing the perturbed temperature to an equilibrium temperature which was assumed to be a linear function of SST (Davey and Gill 1987; Seager 1991; Wang and Li 1993). In reality, the climatological temperature distribution in the middle troposphere differs substantially from the surface temperature pattern (Oort 1983). The longwave radiation is largely determined by clouds and vertical distribution of temperature and moisture. Stephens et al. (1994) indicate that due to the relatively uniform spatial distributions of temperature and moisture in the Tropics, the observed clear-sky longwave radiation cooling has little horizontal gradients. However, the longwave cloud radiative forcing sets up considerable longitudinal radiative heating gradients across the Pacific. The eastern portion of the tropical Pacific is a region of prevalent low cloudiness, and the net column cooling in this region exceeds the clear-sky values due to the large cloud-top outgoing longwave radiation. In contrast to this strong cooling in the eastern portions of the tropical and subtropical Pacific is the weaker cooling in the western Pacific where heating by deep convective cloud systems approximately halve the clear-sky value of the column cooling. The longitudinal and the accompanying meridional radiative heating gradients will increase the rainfall in the deep convective regions, and enhance the Walker circulation and Hadley circulation (Slingo and Slingo 1988; Chen et al. 1995). Nigam's (1997) work on the cold tongue onset in the eastern equatorial Pacific also indicates that the longwave radiative cooling from the developing stratocumulus cloud is important for the seasonal strengthening of the southerly cross-equatorial surface wind. These results strongly suggest that the cloud-longwave radiation forcing plays an important role in driving tropical circulations, but it was misrepresented in the previous intermediate models.

In order to represent longwave radiative process realistically and keep, at the same time, the model's low vertical resolution and computational efficiency, a radiative transfer scheme analogous to Arakawa et al. (1969) is introduced. This scheme is based on an empirical transmission function that primarily depends on a column water vapor amount. Clouds are simply treated as opaque black bodies for longwave radiation. The formulations of Arakawa's scheme are presented in detail in the Rand Corporation report of Gates et al. (1971). A brief description of the scheme is given in the appendix.

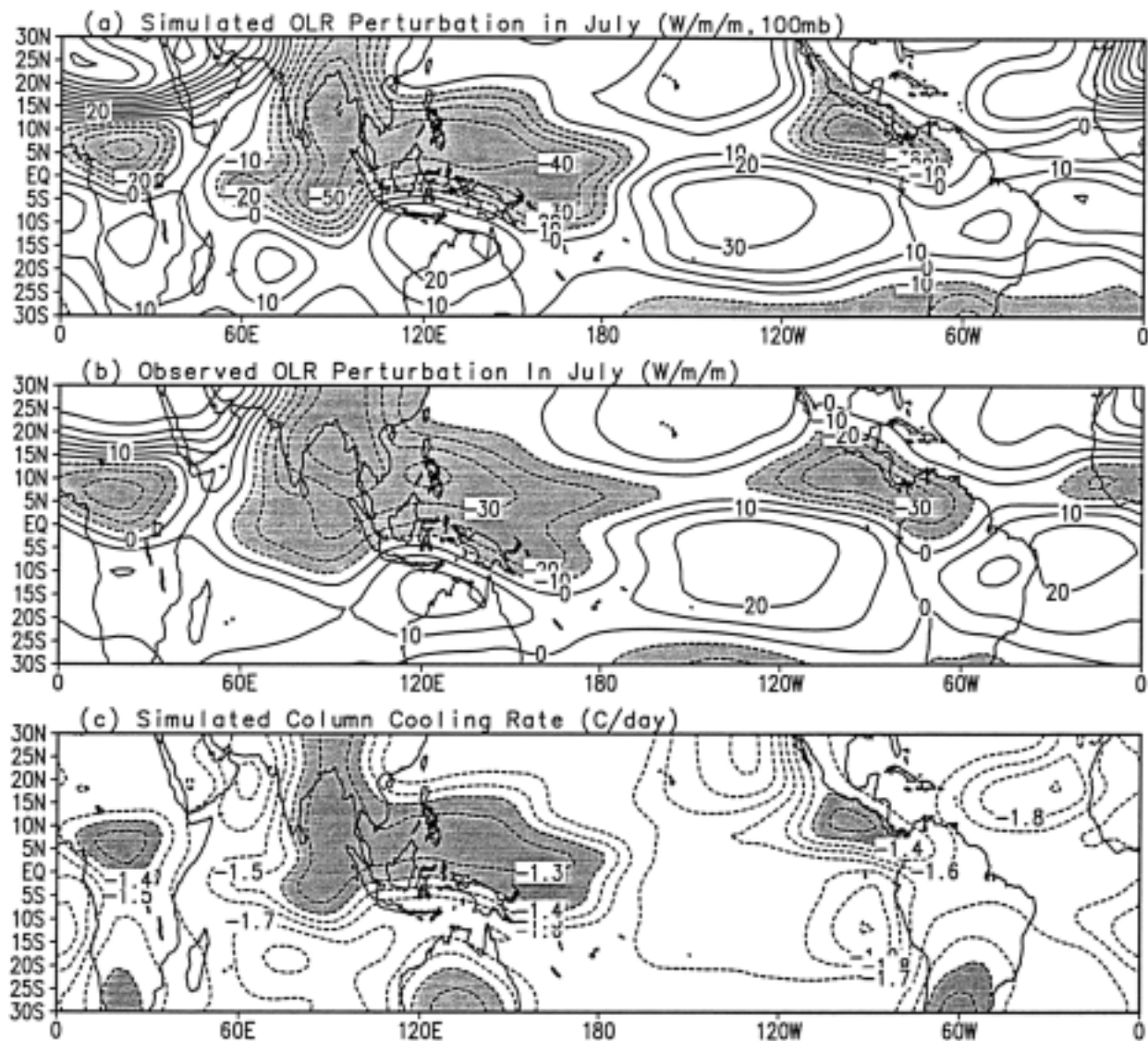Three types of clouds are incorporated into the present

FIG. 4. (a) The July mean OLR perturbations (total − 220) (W m^{-2}) derived from the model and (b) from the satellite observation (total − 250), and (c) the column longwave radiation cooling rate (C day^{-1}) simulated by Arakawa et al. (1969) longwave radiation scheme.

model: the high, middle, and low clouds that are, respectively, defined by the cloud top temperature as below 260 K, between 260 and 280 K, and above 280 K. The cloud data used to estimate longwave radiative cooling are derived from International Satellite Cloud Climatology Project (ISCCP, Rossow et al. 1988). The simulated outgoing longwave radiation (OLR) perturbations in July (Fig. 4a) agree quite well with the observations (Fig. 4b). In both the simulation and observation, negative perturbations occur over the deep convective regions (North Africa, North Indian and Western Pacific Oceans, and Northeast Pacific warm pool); positive perturbations exist in the subtropics and eastern Pacific and Atlantic Oceans with the maximum over the North African desert region. The simulated column cooling rate (Fig. 4c) is also quite similar to the obser-

vations of Stephens et al. (1994) in both the magnitude and the spatial pattern. The difference in the mean (30 W m^{-2}) of the simulated and observed OLR is due to the fact that our model top is set at 100 hPa, and the corresponding OLR should be smaller than that at the top of the atmosphere (~0 hPa, Feiglelson et al. 1991).

b. Sensitivity of tropical circulations to cloud–longwave radiation forcing

The effects of cloud-longwave radiation forcing on the tropical surface winds are demonstrated in this section. To facilitate comparison, the model boundary layer keeps the same as in Wang and Li (1993).

The simulated surface winds and corresponding discrepancies with observations are shown in Figs. 5a,b.
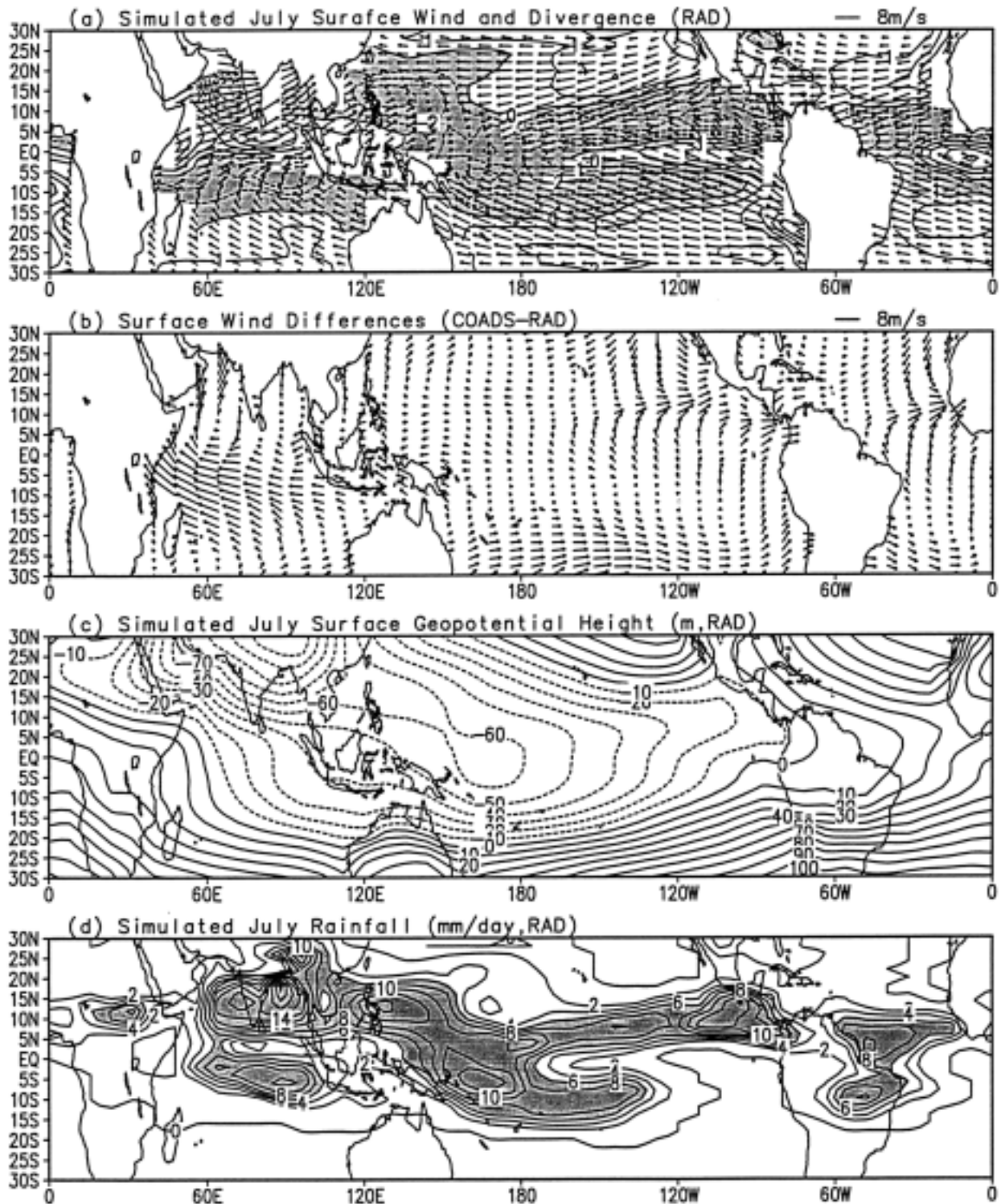
FIG. 5. Same as Fig. 3, except using the improved longwave radiation scheme.

The most obvious improvement of the surface winds comparing with the WL93 results (Figs. 3a,b) is the enhancement of northeast trades that extend westward into the western ocean basins. The corresponding sur-

face geopotential height (Fig. 5c) shows westward extension of subtropical highs over both the North Pacific and North Atlantic Oceans. The enhanced subtropical highs and northeast trades result from the increased ra-
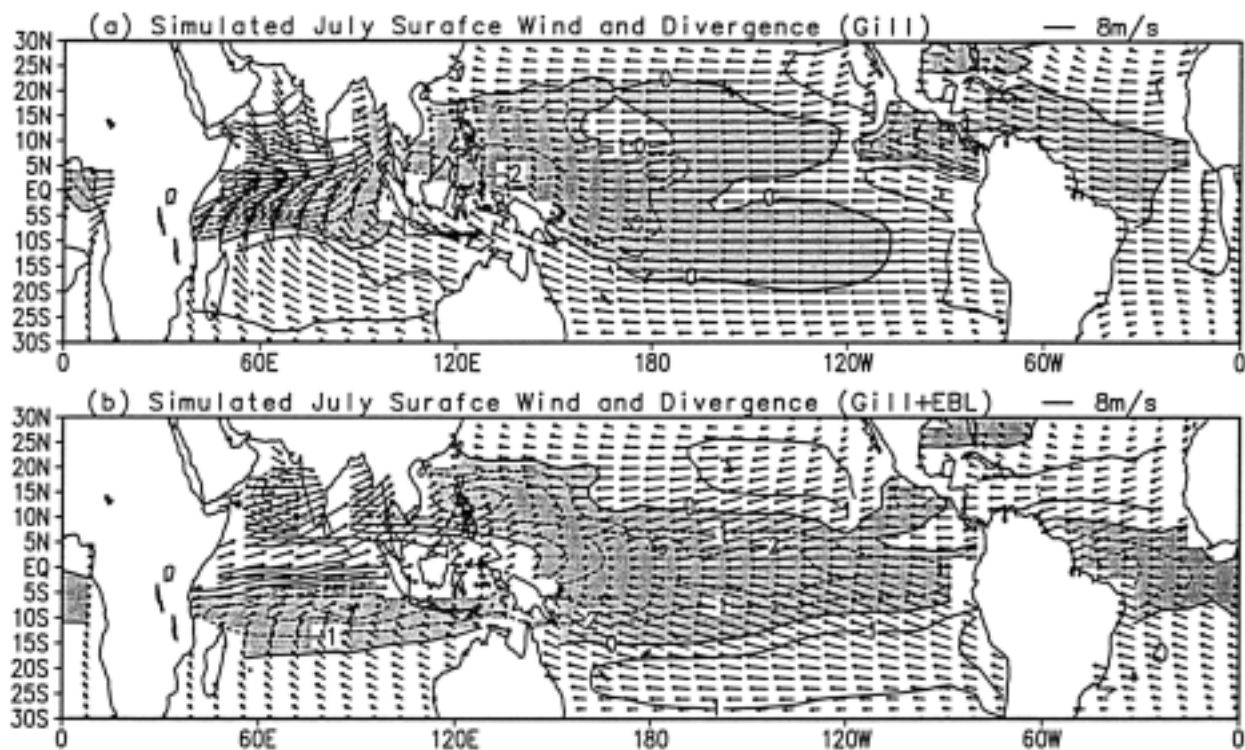
FIG. 6. (a) July mean surface winds and divergence simulated by a Gill-type model and (b) a Gill-type model combining with an Ekman boundary layer (no SST gradient forcing).

diative cooling due to the in situ high SST and low cloudiness.

Other improvements include an increase of the cross-equatorial southeast trades over the central Pacific and an increase of the southwest monsoon in the northern Indian Ocean. The former is induced by the enhanced longitudinal and meridional cloud-longwave radiative cooling gradient (Fig. 4c). The latter are associated with the dramatic deepening of the South Asia monsoon trough (Figs. 3c and 5c), which enhances the north–south pressure gradients and southwest monsoon flows. Why is the monsoon trough much deeper with the new longwave radiation scheme? As has been pointed out in the previous section, in the rainy region, latent heat release warms the atmosphere and lowers SLP. The previous model's Newtonian cooling tends to reduce atmospheric warming and prohibit decrease in SLP. The present longwave radiation scheme removes this erroneous constraint, so that latent heat released in the precipitation region effectively deepens the monsoon trough. Associated with the improved surface winds is the better simulated precipitation field (Fig. 5d). The rainfall in the western North Pacific monsoon trough and Indian monsoon trough are much enhanced (cf. Figs. 3d and 5d) and compare favorably with observations (Fig. 2c).

Although the northeast trades as a whole are improved, the trades in the neighborhood of the Pacific and Atlantic ITCZs still have some significant discrep-

ancies with the observations. This may be partially related to the deficiencies in the model's oversimplification of the boundary layer. We should note also that these regions are confluent zones between the southeast and northeast trades, even the two datasets (COADS and ECMWF analysis) show considerable differences of the surface wind speed in these regions (maximum discrepancy reaches about 4 m s^{-1}).

4. The role of the planetary boundary layer

a. Effects of boundary layer dynamics

The boundary layer processes in the WL93 model play a critical role in simulating surface winds and convergence. If we remove the boundary layer from the WL93 model, a Gill-type model results. Even with the new longwave radiation scheme, the simulated July mean surface winds and divergence (Fig. 6a) are very different from those with the boundary layer (Fig. 5a). The convergence in the ITCZs of the Pacific and Atlantic Oceans becomes very weak, while excessively large low-level convergence occurs over the equatorial Indian Ocean. This suggests that a single-baroclinic-mode model with self-sustained heating is unable to reproduce reasonable surface winds over the monsoon and ITCZ regions.

In the WL93 model, the boundary layer dynamics includes two major processes. First, the boundary layer

friction induces moisture convergence which supplies "fuel" for the free atmospheric latent heating release. Second, the boundary layer flow is affected by SST gradients. To identify the role of the equatorial β-plane Ekman dynamics on surface wind simulation, we first neglect SST gradient forcing and boundary layer thermodynamics but add a linear slab Ekman layer into a Gill-type model. The surface geopotential perturbation is assumed to be the same as that of the lower troposphere (Wang and Li 1994). The governing equations for surface winds u_s and v_s are

$$\frac{\partial u_s}{\partial t} - \beta y v_s = -\frac{\partial \Phi}{\partial x} + F_x + K_H \nabla^2 u_s, \quad (4.1)$$

$$\frac{\partial v_s}{\partial t} + \beta y u_s = -\frac{\partial \Phi}{\partial y} + F_y + K_H \nabla^2 v_s, \quad (4.2)$$

where Φ is the lower-tropospheric geopotential perturbation; β and y denote, respectively, the meridional gradient of the Coriolis parameter at the equator and the meridional distance from the equator (northward is positive); K_H is the horizontal diffusion coefficient (2.5×10^5 m^2 s^{-1}, Chang 1977), and F_x and F_y represent vertical momentum mixing

$$F_x = \frac{1}{\rho} \frac{\partial \tau_x}{\partial z}, \qquad F_y = \frac{1}{\rho} \frac{\partial \tau_y}{\partial z}, \quad (4.3)$$

where τ_x, τ_y denote the vertical turbulent momentum fluxes which decrease with height z in the frictional layer (depth H_i) following the empirical formula (Caughey and Palmer 1979)

$$\tau_x = \tau_{sx}\left(1 - \frac{z}{H_i}\right)^2, \qquad \tau_y = \tau_{sy}\left(1 - \frac{z}{H_i}\right)^2, \quad (4.4)$$

where the surface turbulent momentum fluxes τ_{sx}, τ_{sy} are estimated using bulk aerodynamic formula. For surface winds, $z/H_i \ll 1$, we have

$$F_x = -\frac{2\tau_{sx}}{\rho H_i} = -\frac{2C_D V_s}{H_i} u_s,$$

$$F_y = -\frac{2\tau_{sy}}{\rho H_i} = -\frac{2C_D V_s}{H_i} v_s, \quad (4.5)$$

where V_s is the surface resultant wind. If we write $F_x = -\varepsilon_s u_s$, $F_y = -\varepsilon_s v_s$, then $\varepsilon_s = 2C_D V_s/H_i$. Taking $C_D = 0.5 V_s^{0.5} \, 10^{-3}$ (Wu 1969) and $H_i = 1$ km, ε_s averaged over the entire tropical ocean is about 1.8×10^{-5} s^{-1}, which is comparable to observations (Blanc 1985). Over land, due to the large roughness length, the surface friction coefficient ε_s is assumed to be doubled if the topography is lower than 500 m and multiplied by a factor $h/500$ (h is topographic height in meters) with topography higher than 500 m to reflect the mountain friction (Garratt 1977).

The interaction between boundary layer flow and the free troposphere is described in the same manner as in Wang and Li (1994). The low-tropospheric pressure gradient drives the boundary layer flows whose convergence supplies moisture to convection. The latent heating released in the free-tropospheric convection forces free-tropospheric circulation and changes the lower-tropospheric pressure; the latter feeds back to the boundary layer flows. Figure 6b shows the simulated July mean surface winds and divergence. The divergence fields in the Indian sector are better simulated comparing with the Gill model (Fig. 6a). The observed convergence zones (Fig. 2a) over the Arabian Sea, Bay of Bengal, and immediately south of the equator are realistically reproduced. This is due to two reasons. First, the large boundary layer friction over Indian subcontinent tends to generate PBL convergence northward of the free-tropospheric convergence that is shown in Fig. 6a. Second, due to the shift of the convergence areas between the PBL and the free troposphere, the latent heat release associated with the boundary layer convergence is able to effectively decrease the lower-tropospheric geopotential through the positive feedback between the convective heating and boundary layer frictional convergence. These two processes have been well demonstrated for the development of the tropical intraseasonal system by Wang and Li (1994).

The boundary layer friction displaces the equatorial Indian Ocean convergence in the Gill model northward, yielding a better simulation of the monsoon trough. But, the ITCZ in the Pacific and Atlantic Oceans remains a missing feature (Fig. 6b). Comparison of Fig. 5a (with PBL SST gradient forcing) and Fig. 6b indicates that the SST gradient forcing dramatically enhances the convergence in the ITCZs of the Pacific and Atlantic Oceans, because the boundary layer pressure gradient force induced by meridional SST gradients in each side of the ITCZ supports stronger meridional wind convergence.

b. Effects of boundary layer thermodynamics

Although the simulation of the ITCZ is much improved after including the SST gradient forcing in the PBL, a spurious convergence zone appears in the immediate south of the equatorial cold tongues over the Pacific and Atlantic Oceans (Fig. 5a). As indicated in section 2, this might be caused by the exaggerated SST gradient forcing on the surface flows. In original WL93 model, the mixed-layer air temperature is equal to the underlying SST, which assumes the surface heat flux is the only important term in the boundary layer. However, the mixed-layer air temperature is not only affected by the vertical mixing, but also by advection, longwave radiation, and horizontal diffusion.

In order to incorporate the above processes into the PBL thermodynamics, a bulk boundary layer is considered for simplicity. The governing equation in pressure coordinates, after use of hydrostatic balance and neglect of the horizontal advection and vertical turbulent flux at the top of the PBL, is

$$\frac{\partial \Phi_d}{\partial t} + \Delta p_e S_b \omega_b$$

$$= \frac{R\rho g}{p_3} F_{T_s} - \frac{R\Delta p_e}{p_3 C_p} Q_{rs} + K_H \nabla^2 \Phi_d, \qquad (4.6)$$

where the geopotential thickness $\Phi_d = \Phi_s - \Phi_e$; Φ_e and Φ_s stand for the geopotential at the top and bottom of PBL, respectively; Δp_e ($= p_s - p_e$) is the PBL depth; S_b the mean static stability parameter in the PBL ($S_b = 0.87 \times 10^{-6}$ m^2 s^{-1} P_a^{-2}); g, R, and C_p denote, respectively, the gravity, gas constant of air, and specific heat at constant pressure; ω_b the vertical pressure velocity at p_3, which is obtained from the surface winds using continuity equation; the values of p_s, p_e, p_3 can be found in Fig. A1; Q_{rs} is the boundary layer longwave radiation heating rate; and F_{Ts}, the surface heat flux, is expressed as

$$F_{Ts} = C_H V_s (T - T_s), \qquad (4.7)$$

where C_H denotes the bulk sensible heat exchange coefficient, which is taken to be 1.3×10^{-3} over ocean (Blanc 1985) and doubled over land in accordance with larger roughness length.

The model with the new longwave radiation and boundary layer thermodynamics is referred to as WLF97. The simulated July mean surface winds and divergence, sea level geopotential height, and rainfall are presented in Fig. 7. A comparison of Figs. 5 and 7 would reveal the effects of the PBL thermodynamics. Inclusion of the PBL thermodynamics improves the simulation of surface winds primarily in the near-equatorial regions, where the winds are very sensitive to changes in surface pressure (Figs. 5b and 7b). The southeast trades in the southwest Indian Ocean and the cross-equatorial southeast trades south of the ITCZs in the eastern Pacific and Atlantic show smaller discrepancies with observations. The subtle changes in surface winds can be better seen from the simulated surface divergence fields (Figs. 5a and 7a). Without PBL thermodynamics (Fig. 5a), there were spurious surface convergence zones south of the equator over the eastern Pacific and Atlantic Oceans that are eliminated by the incorporation of PBL thermodynamics (Fig. 7a). This can also be seen from the distributions of the simulated surface geopotential height (Fig. 7c). For example, over the Indian Ocean, the pressure ridge along the eastern African coast and in the equatorial Indian Ocean in Fig. 5c disappears. As a result, the southeast trades in the southwest Indian Ocean are enhanced. Similarly, over the eastern equatorial Pacific and Atlantic Oceans, the location of the near-equatorial trough is better simulated (Fig. 7c).

The above improvements over the cold tongue regions and the southwest Indian Ocean are attributed to the removal of an overestimated SST gradient forcing on the PBL flows. To demonstrate this, we compute the PBL geopotential height perturbations in the WL93 and in the WLF97 model which are compared with the corresponding ECMWF analysis in Fig. 8. In the WL93

model, the pressure ridges associated with the underlying SST cold tongue are clearly seen over the Somali coast, and the equatorial eastern Pacific and Atlantic Oceans (Fig. 8a). They are artifacts of the exaggerated SST gradient forcing in the slab boundary layer. Obviously, the incorporation of PBL thermodynamics leads to an improved surface pressure field over the cold tongue regions (Fig. 8b).

To identify the dominant PBL processes that contribute to the above improvements, we have conducted additional sensitivity experiments. The PBL longwave radiation is found unimportant. After including the horizontal temperature advection and excluding the horizontal diffusion in Eq. (4.6), the modeled results are very similar with the control run. However, if the vertical temperature advection (the adiabatic term) in Eq. (4.6) is excluded, the simulated surface convergence and divergence (figure not shown) are excessively large especially near the equatorial regions, suggesting that the PBL adiabatic term is important in this model to offset the sensible heating effect on PBL air temperature and in reducing the exaggerated SST gradient forcing on surface flows. This is because in the surface convergence zones (high SST), the adiabatic cooling associated with ascending motion acts to cool the boundary layer, opposing the effect of sensible heating, but in the surface divergence zones (low SST), the adiabatic warming associated with descending motion tends to warm the boundary layer. If we increase the horizontal diffusion coefficient in Eq. (4.6) from 2.5×10^5 to 4×10^6 m^2 s^{-1} (Gill 1982; Seager et al. 1995), even without the vertical temperature advection, the modeled divergence and convergence fields near the equator also show significant improvement through smoothing the spatial temperature gradient. We should note, however, the large horizontal diffusion coefficient of Gill (1982) is deduced from the midlatitude heat flux transport due to transient eddies. There is no observed evidence to support such a large horizontal diffusion coefficient in the Tropics.

5. Simulation of the annual cycle and interannual variations of the tropical climate

a. Annual variations

As shown in Fig. 7a, the WLF97 model reproduces realistic July mean northeast trades and the cross-equatorial southeast trades over the Pacific and Atlantic Oceans. The Atlantic northeast trades extend well into the Caribbean Sea, which is falsified in most previous intermediate models. Over the Indian Ocean, the southeast trades and the southwest monsoons are also simulated reasonably well. A major discrepancy is found in the equatorial Indian Ocean where the model produces a fictitious belt of northward flow along the central-eastern equatorial Indian Ocean (Fig. 7b). This reduces the surface convergence just south of the equator.
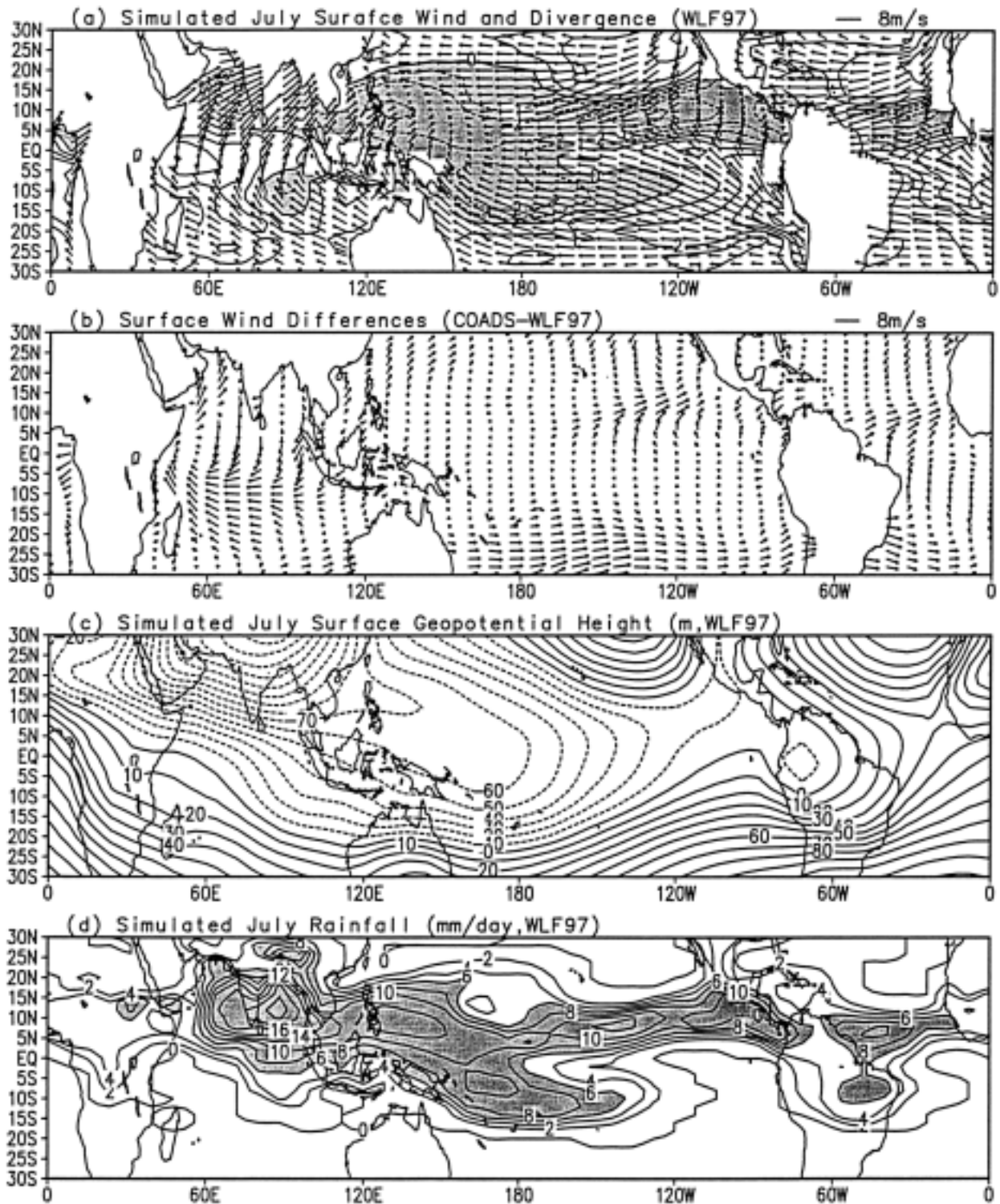
FIG. 7. Same as in Fig. 3, except with the improved longwave radiation and planetary boundary layer thermodynamics (WLF97 model).
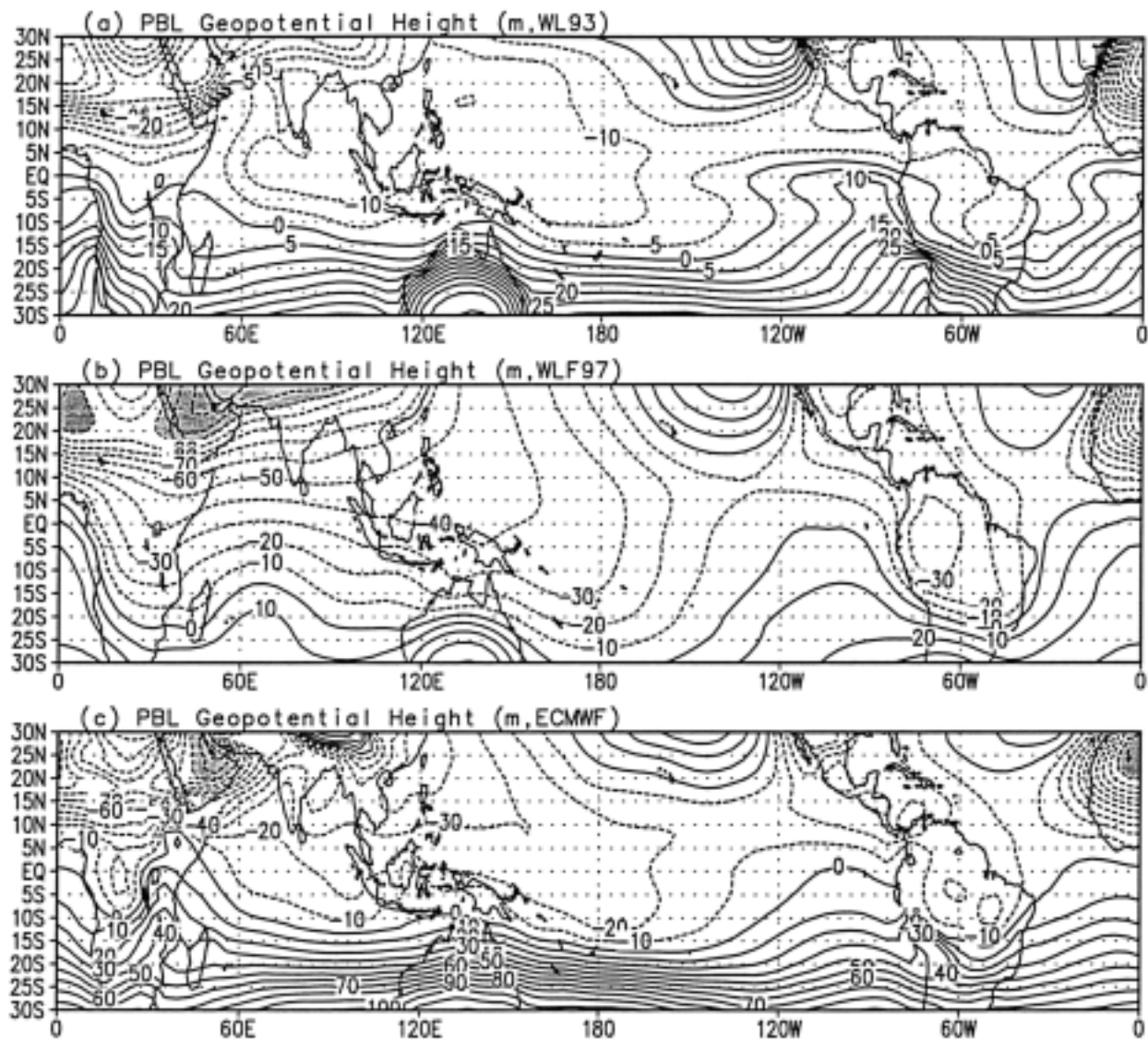
FIG. 8. (a) The boundary layer geopotential height perturbations from WL93, (b) from WLF97, and (c) from ECMWF analysis. The contour interval is 10 m for (b) and (c) but 5 m for (a); the areas with values less than −100 m are shaded.

Another discrepancy in wind simulation is found over the southern Pacific subtropical region: the easterlies were excessively strong. This is due to the lack of baroclinic eddies in the model. In July, these transients are active in the southern subtropical region, which transport westerly momentum toward the Tropics. The large-scale tropical rainfall pattern (Fig. 7d) bears resemblance to observations (Fig. 2c). Over Africa, the modeled rainfall is centered at the Northern Hemisphere, but confined to south of 15°N. The amounts of rainfall in the western North Pacific monsoon trough, SPCZ, and ITCZ are comparable with the observations.

The January mean climate reproduced by the WLF97 model is presented in Fig. 9. In general, the trades over the Atlantic and Pacific and the monsoons over the In-

dian Ocean and the western Pacific, along with the major oceanic convergence zones, are well captured. A major discrepancy is the missing westerlies in the North Pacific subtropics (north of 20°N), which is due to the lack of midlatitude westerly transient effects in the model. The simulated rainfall pattern in January (Fig. 9d), including the heavy rainfall over Southern Africa, the South Indian ocean convergence zone, SPCZ, and South America and the ITCZ is comparable with Xie and Arkin's (1996) analysis (Fig. 9c).

For coupled atmosphere–ocean climate models, accurate simulation of equatorial winds is critical. In Figs. 10a,b, we compare observed and simulated annual variations of equatorial zonal winds. The all-year-round westerlies in the eastern Indian Ocean and the annual
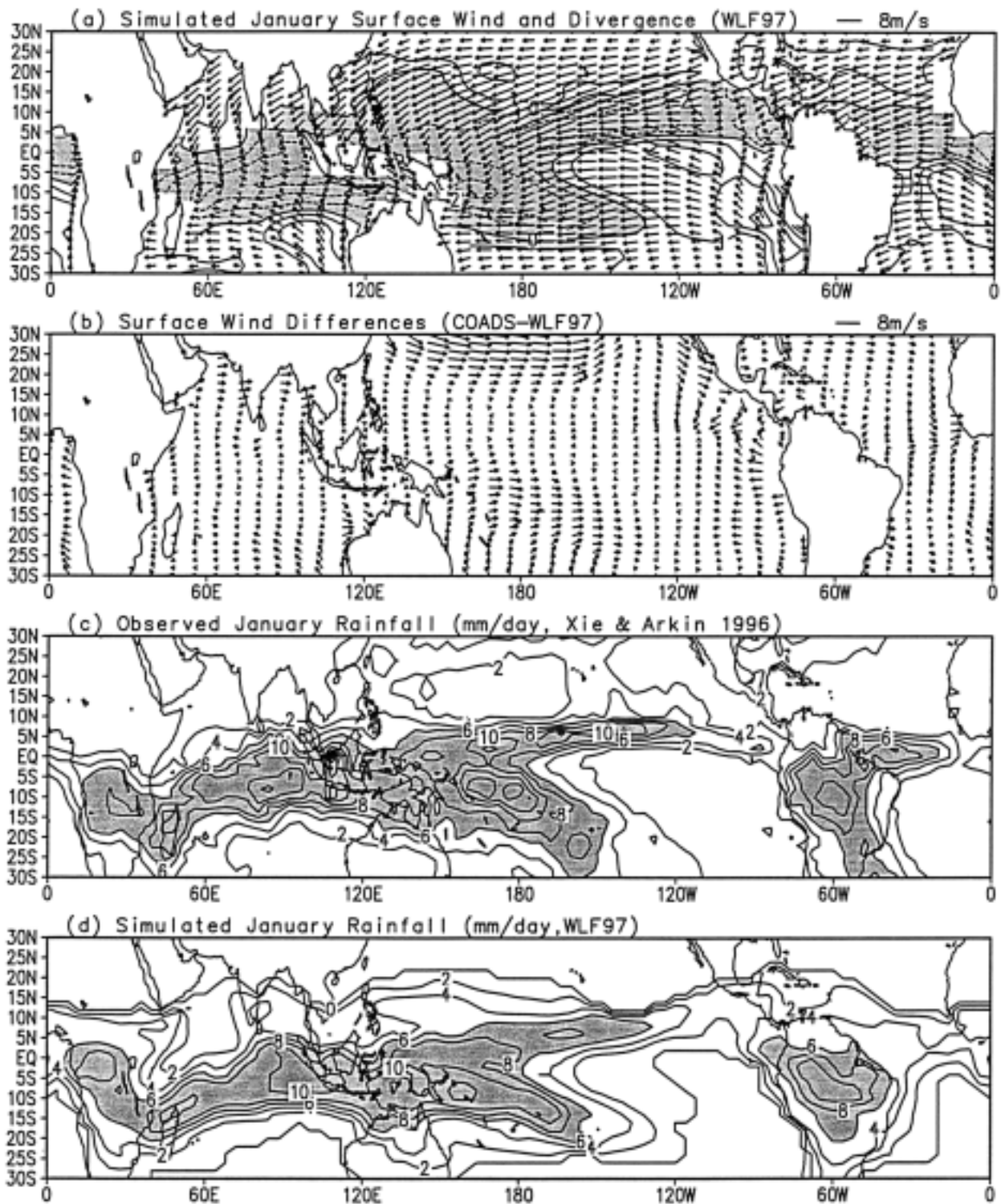
FIG. 9. (a) Simulated surface winds and divergence, (b) the differences between the modeled surface winds and observations, (c) observed, and (d) simulated precipitations in January. The observed winds and precipitation are, respectively, from Sadler et al. (1987) and Xie and Arkin (1996). The model used is WLF97.
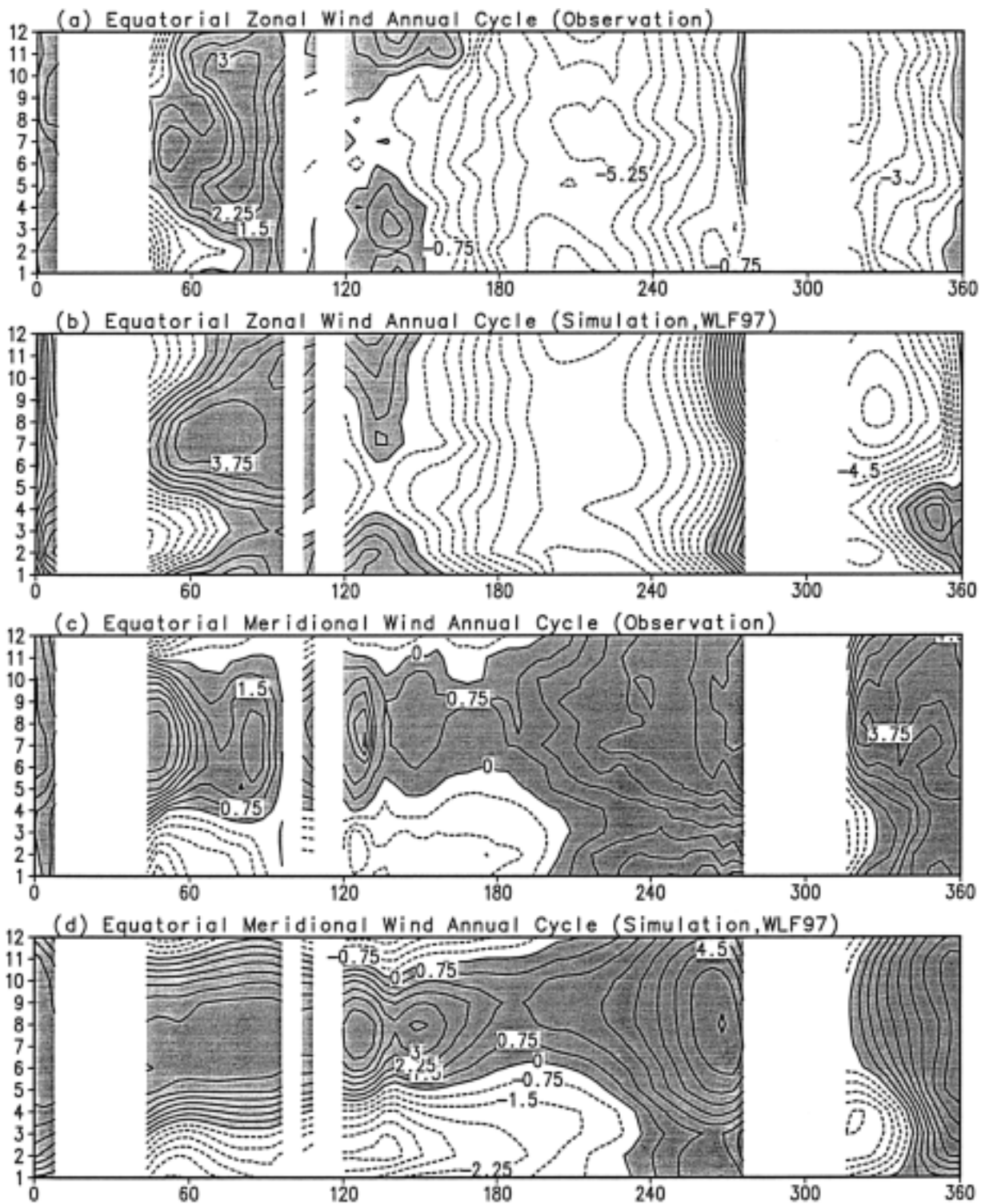
FIG. 10. (a) Observed and (b) simulated zonal flows, and (c) observed and (d) simulated meridional flows at the equator as functions of longitude and time. Contour interval is 1 m s^{-1} (shading for the westerly and southerly winds).

reversal of monsoons in the western Indian Ocean are reproduced faithfully, but the simulated equatorial summer westerlies along the equatorial Indian Ocean are stronger than the observed. In the western Pacific, the zonal wind reversal between summer easterlies and winter westerlies is well captured except that the boreal spring transition occurs one to two months earlier. Over the central Pacific (180°–130°W), the weakest easterlies in boreal spring are well modeled. A major discrepancy is seen near the South American coast where the simulated westerlies are much too strong throughout the year. In the Atlantic sector, the all-year-round coastal westerlies over Gulf of Guinea and the weakest boreal spring trades in the equatorial Atlantic are realistic, but the April–May westerlies are not observed. The same problem occurs in Seager and Zebiak's (1995) simulation.

Figures 10c,d compare the observed and simulated cross-equatorial winds. The overall performance appears to be better than the zonal wind component. The meridional winds are controlled by hemispheric thermal contrast while the zonal winds are controlled by longitudinal contrast between the ocean and land. The latter are more difficult to handle in the model. An interesting feature is the establishment of southerlies in the Eastern Hemisphere occurs progressively later from African coasts eastward to the date line. In the Western Hemisphere, the northward wind persists throughout the year, implying that the ITCZ is always located in the Northern Hemisphere. All the above basic features along with the timing of maximum northward cross-equatorial flows in three tropical oceans are well simulated. Because the cross-equatorial meridional wind component is argued to be critical to the annual evolution of the cold tongue–ITCZ complex (Mitchell and Wallace 1992; Wang 1994), the faithful simulation of the cross-equatorial flow over the eastern Pacific with this intermediate atmospheric model provides an improved simulation of the cold tongue annual cycle when it is coupled with an ocean model.

b. Interannual variations

Since the strongest interannual variations of the SST over the Tropics are located in the eastern tropical Pacific, in the following experiment, only the interannual variations of SST over the tropical Pacific are considered. Outside the tropical Pacific, the underlying surface temperature keeps a fixed annual cycle. The anomalous SST forcing is derived from ECMWF analysis. The cloud cover used here contains the climatological annual cycle, but not the interannual variations.

Figure 11 presents the model simulated equatorial zonal wind and rainfall anomalies in comparison with the observed equatorial zonal wind (ECMWF analysis) and OLR anomalies. Evidently, the large-scale wind and rainfall anomalies are well captured in both the warm (1986–87, 1991–92) and cold (1988–89) phases. The

rainfall anomalies, representing atmospheric heat sources, are located to the west of the SST anomalies in both the observation and simulation. The spatial distributions of simulated surface wind and rainfall anomalies over the tropical Pacific are presented in Fig. 12 along with the observed counterparts (here, the negative OLR anomaly is used to surrogate positive rainfall anomaly). The 3-month mean for August, September, and October in 1987 has been taken as the representative of the peak warm phase during which the observed anomalous winds converge to the warm SST mainly from the west and north. The observed anomalies over the southeast Pacific near the model boundary are not reproducible in the model. These anomalies may arise from the mid-latitude influences.

The simulated atmospheric anomalous heating represented by the anomalous precipitation exhibits obviously westward shifts from the underlying SST anomalies. The modeled surface wind anomalies also show strong asymmetry with respect to the equator and between the east and west. These phenomena are captured by this model mainly because the zonal moisture gradient and the dependence of convective heating on total SST have been better represented.

6. Summary

Tropical atmospheric climate model with intermediate complexity (intermediate tropical climate model) is characterized by its relevance to the essential climate dynamics, high computational efficiency, and capability of realistic simulations of the key variables for the coupled climate system. Adequate description of all but only essential physical processes under the constraints of a limited degree of freedom is the principle of developing the intermediate models. Along this line, we have identified two major problems with the existing intermediate climate models: inadequate representation of cloud-longwave radiational forcing and the boundary layer SST gradient forcing.

We have demonstrated that the cloud-longwave radiational forcing should be regarded as an important driving force for tropical surface winds in addition to convective heating and PBL SST gradient forcing. It is an important forcing for the formation of the subtropical high–northeast trades and monsoon trough–southwesterly monsoons. The popularly used Newtonian cooling formulation in previous intermediate models is shown to be particularly inadequate over the trade wind regions with high SST and low cloud fractions (such as the western North Pacific and Atlantic Oceans) and over the monsoon regions with heavy rainfall (such as the South Asia and western Pacific monsoon troughs). Besides, the PBL dynamics (frictional convergence) acts to effectively lower the surface pressure through the positive feedback between the convective heating and boundary layer frictional convergence in the rainy region; the PBL thermodynamic processes, primarily the
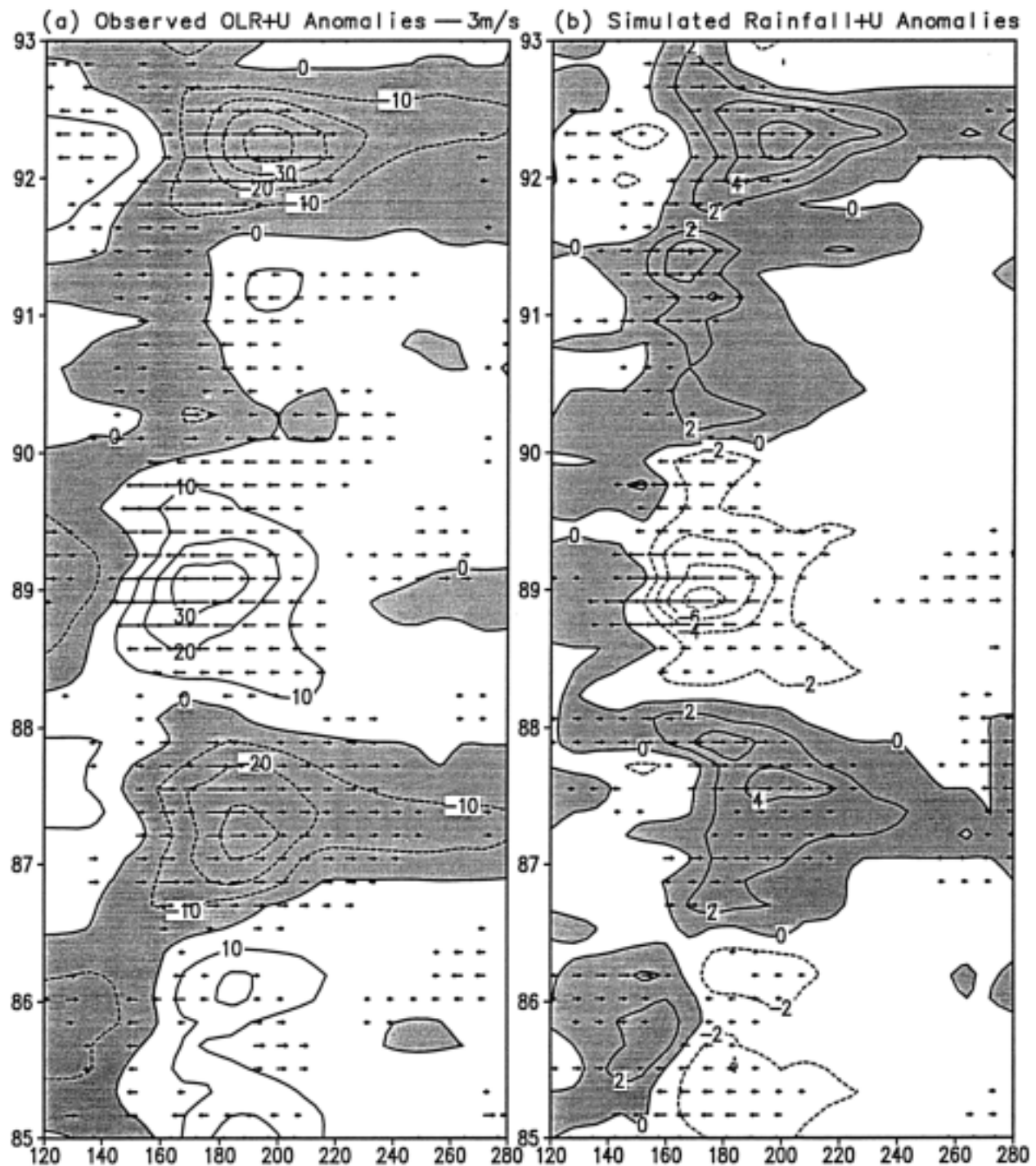
FIG. 11. (a) Observed OLR (with 10 W m^{-2} contour interval, shading for negative anomalies) and zonal wind anomalies (exceeding 0.5 m s^{-1}). (b) Simulated rainfall (with 2 mm day^{-1} contour interval, shading for positive anomalies) and zonal wind anomalies (exceeding 0.5 m s^{-1}) at the Pacific equator from 1985 to 1992. The observed OLR and wind anomalies are, respectively, from COADS and ECMWF analysis.

surface sensible heat flux and vertical temperature advection, are shown to play a significant role in realistic simulations of the intertropical convergence zone (ITCZ) and the surface winds and divergence near the equatorial cold tongue.

The dynamics of the improved intermediate tropical climate model features active interactions between the free troposphere and PBL flows. The PBL flows that are affected by surface heat flux play a dominant role in supplying moist static energy for the latent heat re-
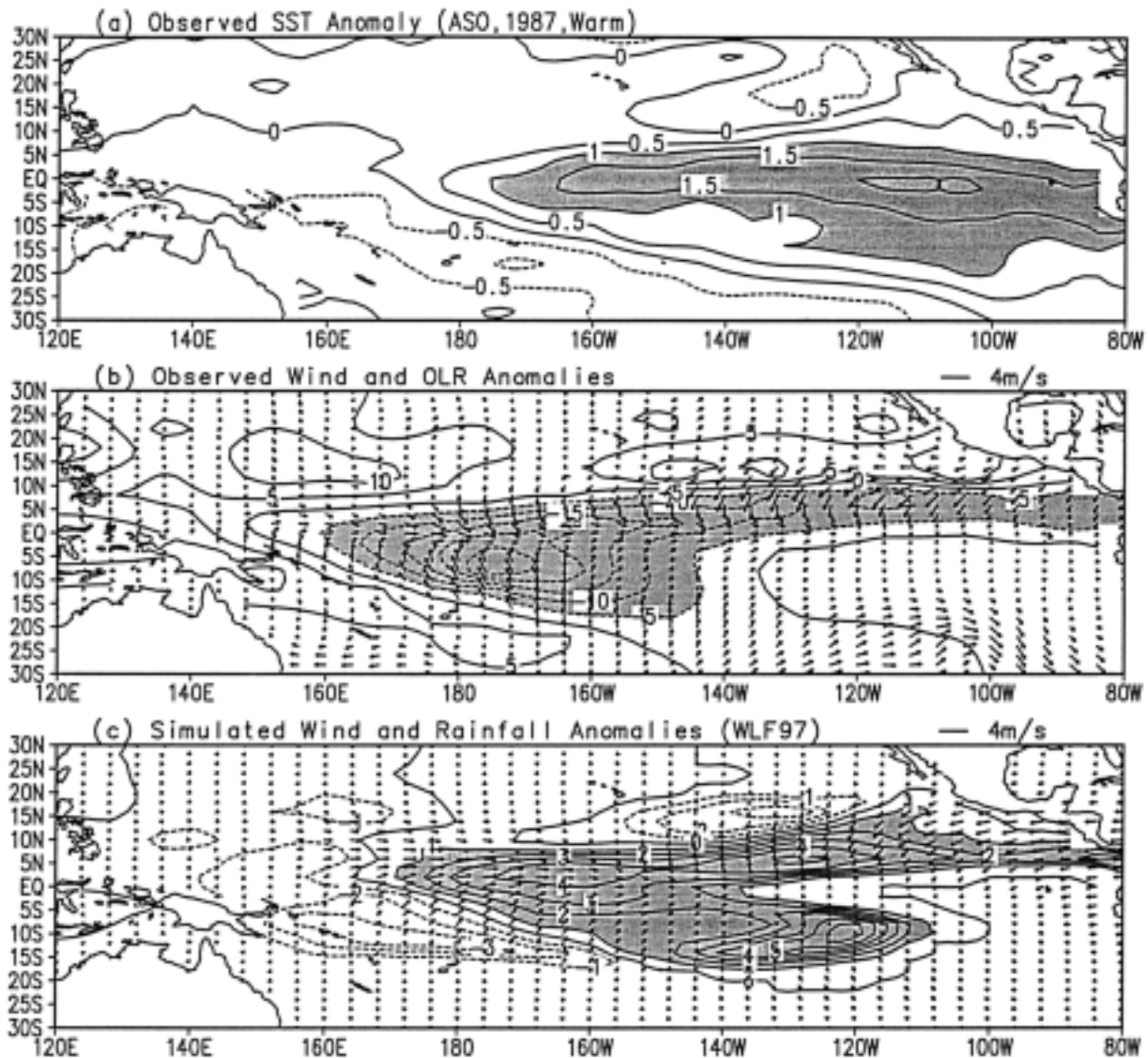
FIG. 12. (a) Observed SST anomalies (from ECMWF analysis) with 0.5°C contour interval and shading for anomalies larger than 1°C. (b) The observed surface wind and OLR anomalies. The OLR contour interval is 5 W m^{-2}. Shading indicates OLR anomalies below -5 W m^{-2}. (c) The simulated surface wind and precipitation anomalies with the WLF97 model. The contour interval for precipitation is 1 mm day^{-1} and the areas larger than 1 mm day^{-1} are shaded. The anomalies are averaged for the period of August–October of 1987 (a warm event).

lease in the free troposphere. The heat source associated with the latent heat release and the heat sink associated with the longwave radiation cooling act together to drive the free troposphere circulations. The change of free tropospheric pressure along with the PBL SST gradient forcing and friction determines the PBL thermal structure and drives the PBL flows.

The model's capability of reproducing both the climatology and interannual variations in surface winds, SLP, and rainfall has been significantly improved, in particular, the summer hemisphere subtropical high and trade winds, the monsoon trough and associated westerly winds, the annual cycle of the equatorial zonal and

cross-equatorial winds, and the anomalous winds and rainfall associated with the interannual variations of SST. Note, however, that longwave radiation in the present model is not interactive with the model's clouds. A necessary step in the near future is to describe interactive cloud-longwave radiation forcing. A simple cloud parameterization scheme such as that of Slingo and Slingo (1988) may offer a hope especially for the deep convective clouds, while the low-level clouds are popularly parameterized as a function of the modeled inversion strength in the GCMs. With this intermediate model it is hard to correctly simulate the PBL top inversion strength due to its linear dynamics and coarse

vertical resolution. However, observations (Oreopoulos and Davies 1993; Klein and Hartmann 1993; Norris and Leovy 1994) indicate that the low-level clouds have good correlation with the underlying SST and divergence in both seasonal and interannual timescales. The parameterization of stratocumulus using SST has shown some success in the simple air–sea coupled model of Li and Philander (1996). The WLF97 model is currently coupled with an intermediate ocean model (Wang et al. 1995) over the tropical Pacific Ocean. This coupling requires high accuracy in equatorial surface wind stress and associated convergence and rainfall. The coupled model's performance on simulating annual cycle and ENSO variability will be assessed and reported later.

APPENDIX

Longwave Radiation Scheme

The longwave radiation scheme of Arakawa et al. (1969) is briefly described in this appendix. Our model's vertical structure is shown in Fig. A1.

At a given level i (p_u, p_e, p_s), the net upward longwave radiation flux can be expressed as

$$R^i = R_A^i + R_B^i, \qquad (A1)$$

where R_A^i is the radiative flux downward from the atmosphere above the level i, R_B^i is the flux from below. They are, respectively, expressed as

FIG. A1. The model's vertical structure for longwave radiation scheme. Note that R_A and R_B [Eqs. (A2), (A3)] in this figure represent the local values, and the same symbol (R_A or R_B) at different places does not necessarily have the same value.

$$R_A^i = \sigma T_i^4 \xi_A, \qquad (A2)$$

$$R_B^i = \sigma(T_s^4 - T_i^4)\xi_B, \qquad (A3)$$

where σ is the Stefan–Boltzman constant (5.6676×10^{-8} W m^{-2} C^{-4}), and the empirical atmospheric transmission functions ξ_A and ξ_B are given by

$$\xi_A = \xi(\mu_\infty - \mu_i), \qquad (A4)$$

$$\xi_B = \frac{1 + \xi(\mu_i)}{2}, \qquad (A5)$$

where $\xi(\mu_i) = 1/(1 + 1.75\mu_i^{0.416})$, and μ_i is the effective water vapor amount per unit area (g cm^{-2}) in the vertical column below a given level i,

$$\mu_i = \frac{1}{g}\int_{p_i}^{p_s} \left(\frac{p}{p_s}\right) q \, dp, \qquad (A6)$$

where specific humidity q is assumed to decay exponentially with height as in Wang (1988).

Under clear-sky condition, using Eqs. (A1)–(A5), we can get the net upward longwave radiative fluxes R_a at p_u, p_e, and p_s, which are represented by R_a^u, R_a^e and R_a^s, respectively, as

$$R_a^u = 0.82\Bigg[\sigma T_u^4 \xi(\mu_\infty - \mu_u) \\ + (\sigma T_s^4 - \sigma T_u^4)\frac{1 + \xi(\mu_u)}{2}\Bigg], \quad (A7.1)$$

$$R_a^e = 0.736\Bigg[\sigma T_e^4 \xi(\mu_\infty - \mu_e) \\ + (\sigma T_s^4 - \sigma T_e^4)\frac{1 + \xi(\mu_e)}{2}\Bigg], \quad (A7.2)$$

$$R_a^s = \sigma T_s^4\{0.6[\xi(\mu_\infty)]^{0.5} - 0.1\}, \qquad (A7.3)$$

where T_s, T_e, and T_u are the temperature at p_s, p_e, and p_u respectively; μ_∞, μ_u and μ_e are the effective water vapor amounts below the top of atmosphere, p_u, and p_e, respectively. The coefficients (0.82, 0.736) in R_a^u, R_a^e, and the modified surface net upward radiative flux R_a^s are empirically introduced to consider the CO_2 effects on the longwave radiation fluxes which are not included in Eqs. (A1)–(A3).

Under fully cloudy sky situations, three sets of formulations are presented for three-type clouds in the model. All clouds are treated as opaque blackbodies (assuming the cloud optical depths are large enough, so that longwave radiation cannot penetrate the clouds). After using Eqs. (A1)–(A5) and referring to Fig. A1, we can get the net upward radiative fluxes R_c at p_u, p_e and p_s for deep convective cloud:
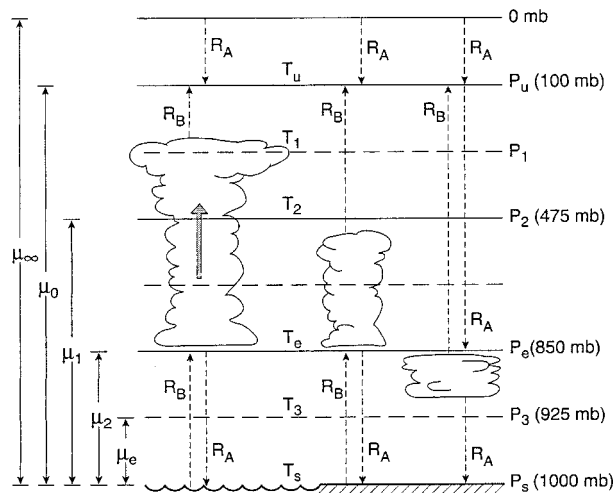
$$R_c^u = 0.82\left[\sigma T_u^4\xi(\mu_\infty - \mu_u)\right.$$

$$\left. + (\sigma T_1^4 - \sigma T_u^4)\frac{1 + \xi(\mu_u - \mu_1)}{2}\right], \quad \text{(A8.1)}$$

$$R_c^e = 0.736(\sigma T_s^4 - \sigma T_e^4)\frac{1 + \xi(\mu_e)}{2}, \quad \text{(A8.2)}$$

$$R_c^s = 0.85(\sigma T_s^4 - \sigma T_e^4)\frac{1 + 3\xi(\mu_e)}{4}, \quad \text{(A8.3)}$$

for middle cloud:

$$R_c^u = 0.82\left[\sigma T_u^4\xi(\mu_\infty - \mu_u)\right.$$

$$\left. + (\sigma T_2^4 - \sigma T_u^4)\frac{1 + \xi(\mu_u - \mu_2)}{2}\right], \quad \text{(A9.1)}$$

$$R_c^e = 0.736(\sigma T_s^4 - \sigma T_e^4)\frac{1 + \xi(\mu_e)}{2}, \quad \text{(A9.2)}$$

$$R_c^s = 0.85(\sigma T_s^4 - \sigma T_e^4)\frac{1 + 3\xi(\mu_e)}{4}, \quad \text{(A9.3)}$$

and for low cloud:

$$R_c^u = 0.82\left[\sigma T_u^4\xi(\mu_\infty - \mu_u)\right.$$

$$\left. + (\sigma T_e^4 - \sigma T_u^4)\frac{1 + \xi(\mu_u - \mu_e)}{2}\right], \quad \text{(A10.1)}$$

$$R_c^e = 0.736[\sigma T_e^4\xi(\mu_\infty - \mu_e)]/2, \quad \text{(A10.2)}$$

$$R_c^s = 0.85(\sigma T_s^4 - \sigma T_e^4)\frac{1 + 3\xi(\mu_e)}{4},$$

where μ_1 and μ_2 are the effective water vapor amounts below p_1 and p_2, respectively; the T_2 and T_3 are the modeled temperature at p_2 and p_3. In this study, T_e, T_1, and T_u are interpolated from T_3 and T_2 with the assumption that potential temperature θ is linear function of p^k (Gates et al. 1971), where $k = R/C_p$, R and C_p denote the gas constant of air and the specific heat at constant pressure. As in the clear-sky case, the coefficients (0.82, 0.736, 0.85) and the modifications to surface net upward longwave radiation flux R_c^s are introduced to consider the CO_2 effects. The flux at p_e for the low cloud is divided by two because the low-cloud top is assumed to be an irregular surface lying half-above, half-below level p_e.

In partly cloudy situations, the net upward longwave radiation flux at level i is expressed as

$$R^i = (1 - \text{cl})R_a^i + \text{cl}R_c^i, \quad \text{(A11)}$$

where cl denotes cloud fractions. The free tropospheric longwave radiative heating rate is

$$Q_r = \frac{1}{m_u}(R^e - R^u), \quad \text{(A12)}$$

where m_u is the weight per unit area (kg m^{-2}) of the air column from the top of the boundary layer at p_e to the top of the troposphere at p_u; and R^e and R^u are the net upward radiative fluxes at p_e and p_u, respectively. In a similar manner, one can express the boundary layer radiative heating.

REFERENCES

Arakawa, A., A. Katayama, and Y. Mintz, 1969: Numerical simulation of the general circulation of the atmosphere. *Proc. WMO/IUGG Symp. on Numerical Weather Prediction in Tokyo,* Tokyo, Japan, Meteorological Society of Japan, IV.7–IV.8.

Benjamin, S. G., and T. N. Carlson, 1986: Some effects of surface heating and topography on the regional severe storm environment. Part I: Three-dimensional simulations. *Mon. Wea. Rev.,* **114,** 307–329.

Betts, A. K., and M. J. Miller, 1986: A new convective adjustment scheme. Part II: Single column tests using GATE wave, BOMEX, ATEX and arctic air-mass data sets. *Quart. J. Roy. Meteor. Soc.,* **112,** 693–709.

——, and ——, 1993: The Betts–Miller scheme. *The Representation of Cumulus Convection in Numerical Models, Meteor. Monogr.,* No. 46, Amer. Meteor. Soc., 107–121.

Blanc, T. V., 1985: Variation of bulk-derived surface flux, stability, and roughness results due to the use of different transfer coefficient schemes. *J. Phys. Oceanogr.,* **15,** 650–669.

Caughey, S. J., and S. G. Palmer, 1979: Some of the aspects of turbulence structure through the depth of convective boundary layer. *Quart. J. Roy. Meteor. Soc.,* **105,** 811–827.

Chang, J., 1977: *General Circulation Models of the Atmosphere.* Academic Press, 337 pp.

Chen, M., R. D. Cess, and M. Zhang, 1995: Effects of longwave cloud radiative forcing anomalies on the atmospheric response to equatorial Pacific sea surface temperature anomalies. *J. Geophys. Res.,* **100,** 13 791–13 810.

Davey, M. K., and A. E. Gill, 1987: Experiments on tropical circulation with a simple moist model. *Quart. J. Roy. Meteor. Soc.,* **113,** 1237–1269.

Deardorff, J., 1972: Parameterization of the planetary boundary layer for use in general circulation models. *Mon. Wea. Rev.,* **100,** 93–106.

Feiglelson, E. M., B. A. Fomin, I. A. Gorchakova, E. V. Rozanov, Y. M. Timofeyev, A. V. Trotsenko, and M. D. Schwarzkopf, 1991: Calculation of longwave radiation fluxes in atmospheres. *J. Geophys. Res.,* **96,** 8985–9001.

Garratt, J. R., 1977: Review of drag coefficients over oceans and continents. *Mon. Wea. Rev.,* **105,** 915–929.

Gates, W. L., E. S. Batten, A. B. Kahle, and A. B. Nelson, 1971: A documentation of the Mintz–Arakawa two-level atmospheric general circulation model. R-877-ARPR, Rand, 408 pp. [Available from Communications Department, Rand, 1700 Main Street, Santa Monica, CA 90406.]

Gill, A. E., 1980: Some simple solutions for heat-induced tropical circulation. *Quart. J. Roy. Meteor. Soc.,* **106,** 447–462.

——, 1982: *Atmosphere–Ocean Dynamics.* Academic Press, 662 pp.

Klein, S. A., and D. L. Hartmann, 1993: The seasonal cycle of low stratiform clouds. *J. Climate,* **6,** 1587–1606.

Kuo, H. L., 1974: Further studies of the parameterization of the influence of cumulus convection on large-scale flow. *J. Atmos. Sci.,* **31,** 1232–1240.

Li, T., and B. Wang, 1994: A thermodynamic equilibrium climate model for monthly mean surface winds and precipitation over the tropical Pacific. *J. Atmos. Sci.,* **51,** 1372–1385.

——, and S. G. H. Philander, 1996: On the annual cycle of the eastern equatorial Pacific. *J. Climate,* **9,** 2986–2997.

Lindzen, R. S., and S. Nigam, 1987: On the role of sea surface temperature gradients in forcing low-level winds and convergence in the tropics. *J. Atmos. Sci.,* **44,** 2440–2458.

Matsuno, T., 1966: Numerical integration of primitive equation by use of a simulated backward difference method. *J. Meteor. Soc. Japan, Sea. II,* **44,** 76–84.

Matthews, E., 1983: Global vegetation of land use: New high-resolution databases for climate studies. *J. Climate Appl. Meteor.,* **22,** 474–487.

Miller, M. J., and A. J. Thorpe, 1981: Radiational conditions for the lateral boundaries of limited area numerical models. *Quart. J. Roy. Meteor. Soc.,* **107,** 615–628.

Mitchell, T. P., and J. M. Wallace, 1992: On the annual cycle in equatorial convection and sea surface temperature. *J. Climate,* **5,** 1140–1156.

Neelin, J. D., 1989: On the interpretation of the Gill model. *J. Atmos. Sci.,* **46,** 2466–2468.

Nigam, S., 1997: The annual warm to cold phase transition in the eastern equatorial Pacific: Diagnosis of the role of stratus cloud-top cooling. *J. Climate,* **10,** 2447–2467.

Norris, J. R., and C. B. Leovy, 1994: Interannual variability in stratiform cloudiness and sea surface temperature. *J. Climate,* **7,** 1915–1925.

Oort, A. H., 1983: Global atmospheric circulation statistics. NOAA Prof. Paper 14, U.S. Government Printing Office, Washington, DC, 180 pp. [Available from GFDL, Princeton, NJ 08542-0308.]

Oreopoulos, L., and R. Davies, 1993: Statistical dependence of albedo and cloud cover on sea surface temperature for two tropical marine stratocumulus regions. *J. Climate,* **6,** 2434–2447.

Reynolds, R. W., 1988: A real-time global sea surface temperature analysis. *J. Climate,* **1,** 75–86.

Rossow, W. B., L. C. Garder, P. J. Lu, and A. Walker, 1988: International Satellite Cloud Climatology Project (ISCCP) documentation of cloud data. WMO/TD 266, World Climate Research Program (ICSU/WMO), 75 pp. [Available from WCRP, WMO, Case Postale 2300, CH-1211, Geneva 2, Switzerland.]

Sadler, J. C., M. A. Lander, A. M. Hori, and L. K. Oda, 1987: Tropical marine climate atlas. Rep. UHMET 87-02, Department of Meteorology, University of Hawaii, Honolulu, HI. [Available from Department of Meteorology, HIG350, 2525 Correa Rd., Honolulu, HI 96822.]

Seager, R., 1991: A simple model of the climatology and variability of the low-level wind field in the Tropics. *J. Climate,* **4,** 164–179.

——, and S. E. Zebiak, 1995: Simulation of tropical climate with a linear primitive equation model. *J. Climate,* **8,** 2497–2520.

——, M. B. Blumenthal, and Y. Kushnir, 1995: An advective atmospheric mixed layer model for ocean modeling purposes: Global simulation of surface heat fluxes. *J. Climate,* **8,** 1951–1964.

Shuman, F. G., 1957: Numerical methods in weather predication: II. Smoothing and filtering. *Mon. Wea. Rev.,* **85,** 357–361.

Slingo, A., and J. M. Slingo, 1988: The response of a general circulation model to cloud longwave radiative forcing. Part I: Introduction and initial experiments. *Quart. J. Roy. Meteor. Soc.,* **114,** 1027–1062.

Stephens, G. L., A. Slingo, M. J. Webb, P. J. Minnett, P. H. Daum, L. Kleinman, I. Wittmeyer, and D.A. Randall, 1994: Observations of the earth's radiation budget in relation to atmospheric hydrology. Part 4: Atmospheric column radiative cooling over the world's oceans. *J. Geophys. Res.,* **99,** 18 585–18 604.

Trenberth, K. E., and A. Solomon, 1994: The global heat balance: Heat transport in the atmosphere and ocean. *Climate Dyn.,* **10,** 107–134.

Waliser, D. E., N. E. Graham, and C. Gautier, 1993: Comparison of the highly reflective cloud and outgoing longwave radiation datasets for use in estimating tropical deep convection. *J. Climate,* **6,** 331–353.

Wang, B., 1988: The dynamics of tropical low-frequency waves: An analysis of moist Kelvin waves. *J. Atmos. Sci.,* **45,** 2051–2065.

——, 1994: On the annual cycle in the tropical eastern central Pacific. *J. Climate,* **7,** 1926–1942.

——, and T. Li, 1993: A simple tropical model of relevance to short-term climate variations. *J. Atmos. Sci.,* **50,** 260–284.

——, and ——, 1994: Convective interaction with boundary layer dynamics in the development of a tropical intraseasonal system. *J. Atmos. Sci.,* **51,** 1386–1400.

——, ——, and P. Chang, 1995: An intermediate model of the tropical Pacific Ocean. *J. Phys. Oceanogr.,* **25,** 1599–1616.

Wu, J., 1969: Wind stress and surface roughness at air–sea interface. *J. Geophys. Res.,* **74,** 444–455.

Xie, P. P., and P. A. Arkin, 1996: Analyses of global monthly precipitation using gauge observations, satellite estimates, and numerical model predictions. *J. Climate,* **9,** 840–858.

Zebiak, S. E., 1982: A simple atmosphere model of relevance to El Niño. *J. Atmos. Sci.,* **39,** 2017–2027.

——, 1986: Atmospheric convergence feedback in a simple model for El Niño. *Mon. Wea. Rev.,* **114,** 1263–1271.